Pseudocapacitance of Mesoporous Spinel-Type MCo$_2$O$_4$ (M = Co, Zn, and Ni) Rods Fabricated by a Facile Solvothermal Route

Vijay Kumar,[†] Chinnasamy Ramaraj Mariappan,[*,†,‡] Raheleh Azmi,[§] Dominique Moock,[§] Sylvio Indris,[§] Michael Bruns,[§,∥] Helmut Ehrenberg,[§] and Gaddam Vijaya Prakash[⊥]

[†]Department of Physics and [‡]School of Materials Science and Technology, National Institute of Technology, Kurukshetra, Haryana 136 119, India

[§]Institute for Applied Materials (IAM-ESS) and [∥]Karlsruhe Nano Micro Facility (KNMF), Karlsruhe Institute of Technology (KIT), Hermann-von-Helmholtz-Platz 1, 76344 Eggenstein-Leopoldshafen, Germany

[⊥]Nanophotonics Laboratory, Department of Physics, Indian Institute of Technology-Delhi, New Delhi 110016, India

Ⓢ Supporting Information

ABSTRACT: We present the structural properties and electrochemical capacitance of mesoporous MCo$_2$O$_4$ (M = Co, Zn, and Ni) rods synthesized by a facile solvothermal route without necessity to use templates. The Brunauer−Emmett−Teller specific surface areas of these mesoporous rods are found to be about 24, 54, and 62 m^2 g^{-1} with major pore diameters of about 31, 15, and 9 nm for MCo$_2$O$_4$, M = Co, Zn, and Ni, respectively. X-ray photoelectron spectroscopy and X-ray diffraction studies reveal the phase purity of the samples with a predominant spinel-type crystal structure. The spinel crystal structure with lattice parameters of 8.118, 8.106, and 8.125 Å is obtained for MCo$_2$O$_4$, M = Co, Zn, and Ni, respectively. The transmission electron microscopy study reveals that the mesoporous rods are built by self-assembled aggregates of nanoparticles which are well-interconnected to form stable mesoporous rods. The electrochemical capacitor performance was investigated by means of cyclic voltammetry, galvanostatic charge/discharge cycling, and impedance spectroscopy in a three-electrode configuration. As a result, the spinel-type MCo$_2$O$_4$ rods exhibit high specific capacitances of 1846 F g^{-1} (CoCo$_2$O$_4$), 1983 F g^{-1} (ZnCo$_2$O$_4$), and 2118 F g^{-1} (NiCo$_2$O$_4$) at a scan rate of 2 mV/s. Furthermore, the mesoporous spinel-type metal oxides show desirable stability in alkaline electrolyte during long-term cycling with excellent cycling efficiency.
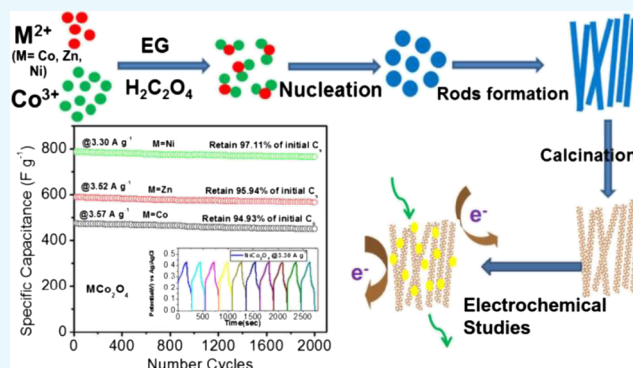
1. INTRODUCTION

Global demand for energy conversion and storage technology is anticipated to rise rapidly because of the depletion of fossil fuels. Therefore, researchers currently focus on developing electrochemical energy storage technologies for sustainable energies by simple, effective, and eco-friendly approaches.[1−5] Supercapacitors are a new category of energy storage devices. They have attracted much attention because of their fast charge/discharge rate, high power density, high reliability, and long life cycle.[6−9] RuO$_2$ has been investigated extensively because of its high specific capacitance (700 F g^{-1}), high reliability, and good reversibility.[10,11] However, the high cost and environmental harmfulness of RuO$_2$ prevent its commercialization in supercapacitors. Hence, various spinel-type binary metal oxides A^{2+}B$_2^{3+}$O$_4$ where A is a divalent cation (Zn, Ni, Mn, Cu, etc.) and B is a trivalent cation (Co, Fe, Mn, etc.) have been recently investigated as pseudocapacitors.[12−21] Among the spinel-type metal oxides, the cobalt-based metal oxides show better electrochemical properties.

Xiong et al. have investigated the pseudocapacitor performance of Co$_3$O$_4$ microspheres, and a specific capacitance (C_s) of 92 F g^{-1} at 5 mA cm^{-2} is reported.[15] Mousavi and co-workers have studied cauliflower-shaped nanostructured CuCo$_2$O$_4$ with the C_s of 338 and 88 F g^{-1} at current densities of 1 and 50 A g^{-1}, respectively.[16] Krishnan et al. have studied the supercapacitance of nanostructured spinel-type MCo$_2$O$_4$ (M = Cu, Mn, and Mg) obtained by the molten salt method. The C_s values of MgCo$_2$O$_4$, MnCo$_2$O$_4$, and CuCo$_2$O$_4$ are 160, 288, and 152 F g^{-1}, respectively, at a current density of 2 A g^{-1}.[17] Zhou et al. have fabricated one-dimensional (1D) ZnCo$_2$O$_4$ porous nanotubes by electrospinning. They have reported the C_s of ZnCo$_2$O$_4$ to be 770 F g^{-1} at a current density of 10 A g^{-1} with excellent rate performance and good cycling stability.[18] Wu et al. have investigated binder-free ZnCo$_2$O$_4$ nanorods on a Ni fiber with a C_s of 10.9 F g^{-1} at 30 mV/s (scan rate).[19] Dong and co-workers

have reported a selective preparation route for hierarchically mesoporous $NiCo_2O_4$ with a C_s of 1619.1 F g^{-1} at a current density of 2 A g^{-1}.[20] Furthermore, the C_s of mesoporous $NiCo_2O_4$ was found to be 571.4 F g^{-1} at a high current density of 10 A g^{-1} with excellent stability. Moreover, the nanostructured spinel-type metal oxides are capable of delivering better electrochemical kinetics because of their larger surface area and shorter paths for charge carrier movement in comparison with their bulk counterparts. On the other hand, it is found that metal oxides with appropriate porous or hierarchical nanostructures can enhance the power density and also the cycling stability of supercapacitors.[20−23] Generally, mesoporous materials are fabricated by using soft templates (surfactants or long-chain polymers) and hard templates (mesoporous silica or carbon).[24−26] However, some complications occur for these methods because of the residual templates in the final samples and the use of multistep procedures.

In this work, we report the preparation of naturally self-assembled porous spinel-type MCo_2O_4 rods (M = Co, Ni, and Zn) by a facile solvothermal method. Structural properties of these samples were investigated by means of powder X-ray diffraction (XRD), thermogravimetric analysis (TGA), X-ray photoelectron spectroscopy (XPS), Raman spectroscopy, scanning electron microscopy (SEM), high-resolution transmission electron microscopy (HR-TEM) with selected area electron diffraction (SAED), and Brunauer−Emmett−Teller (BET) specific surface area analysis. The pseudocapacitance of the mesoporous rods was comprehensively studied for all samples by cyclic voltammetry (CV), galvanostatic charge/discharge (GCD) cycling, and electrochemical impedance spectroscopy in a three-electrode configuration. KOH (6 M) was used as an electrolyte. The electrochemical capacitance C_s was 1846 F g^{-1} for $CoCo_2O_4$, 1983 F g^{-1} for $ZnCo_2O_4$, and 2118 F g^{-1} for $NiCo_2O_4$ at a scan rate of 2 mV/s, and an excellent cycling stability was observed.

2. RESULTS AND DISCUSSION

Figure 1a shows the TGA−differential thermal analysis (DTA) curves for the MCo_2O_4 samples obtained at 80 °C. TG curves show two well-distinct steps of weight loss for all samples. The first weight loss occurs at temperatures up to 190 °C for $CoCo_2O_4$, 184 °C for $ZnCo_2O_4$, and 220 °C for $NiCo_2O_4$ which is due to the evaporation of H_2O. The second weight loss occurring at temperatures up to 300, 405, and 405 °C for $CoCo_2O_4$, $ZnCo_2O_4$, and $NiCo_2O_4$, respectively, is associated with an exothermic peak in the DTA curve (the DTA curve of $CoCo_2O_4$ only shown for clarity) and is assigned to the decomposition of the anhydrous oxalate into spinel-type metal oxides. The evaporation of CO and CO_2 by decomposing the oxalates leads to the formation of porous nanostructured materials. Furthermore, the distribution of pore size and microstructure of the samples are investigated by the Barrett−Joyner−Halenda (BJH) model and HR-TEM. The formation of mesoporous rods is schematically illustrated in Figure 1b. During the initial synthesis process, the divalent (M^{2+} = Co^{2+}/Ni^{2+}/Zn^{2+}) cations and trivalent Co^{3+} cations are interlinked with ethylene glycol (EG) and $H_2C_2O_4$ molecules to form the nanoclusters. Then, a large number of small crystals start to nucleate and form the $MCo_2(C_2O_4)_3$ oxalates which is confirmed by XRD, as shown in Figure 1c. EG acts as a cross-linking reagent to form the rod-shaped products.[30] Finally, the rods are heated in air to transform to the porous spinel-type metal oxide rods by the evaporation of CO and CO_2.
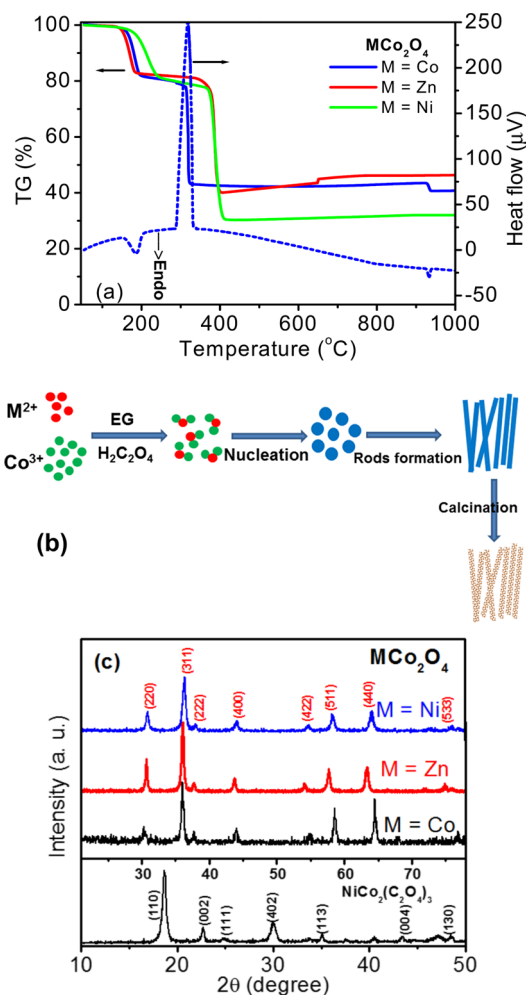
Figure 1. (a) TGA/DTA curves of product precursors. (b) Schematic illustration of the formation of the mesoporous MCo_2O_4 rods where M = Co, Zn, and Ni. (c) XRD pattern of the mesoporous MCo_2O_4 rods.

The XRD patterns of the MCo_2O_4 (M = Co, Ni, and Zn) samples obtained by a facile solvothermal approach and a post-annealing approach at 450 °C for 2 h are shown in Figure 1c. All the peak positions at 2θ values of 31.16°, 36.86°, 38.64°, 44.80°, 55.60°, 59.30°, 65.24°, and 77.42° match well with the spinel-type structure (JCPDS #73-1701), and these peaks correspond to the following Miller indices (hkl): (220), (311), (222), (400), (422), (511), (440), and (533), respectively. These results reveal that the samples contain exclusively the spinel phase. The unit cell parameter a for all samples is determined using the formula $a = d(h^2 + k^2 + l^2)^{1/2}$. The lattice parameters of 8.118, 8.106, and 8.125 Å are obtained for the MCo_2O_4 rods where M = Co, Zn, and Ni, respectively. The (311) peak was used for the calculation of the mean crystallite sizes (D) of the samples by the Debye−Scherrer formula[31] $D = k\lambda/\beta \cos \theta$, where β is the full width at half-maximum of the (311) peak, θ is the Bragg angle, k is the structure factor, and λ = 0.1541 nm is the wavelength. The mean crystallite sizes of 30, 17, and 8 nm are obtained for MCo_2O_4, M = Co, Zn, and Ni, respectively, which are confirmed by TEM analysis.

The morphology of the samples was investigated by SEM. The SEM images of the MCo_2O_4 (M = Co, Zn, and Ni) samples obtained at 450 °C are shown in Figure 2a−c. Bundles of porous rods (log-like structure) are observed for $CoCo_2O_4$ and $ZnCo_2O_4$ (Figure 2a,b), whereas well-defined needlelike rods
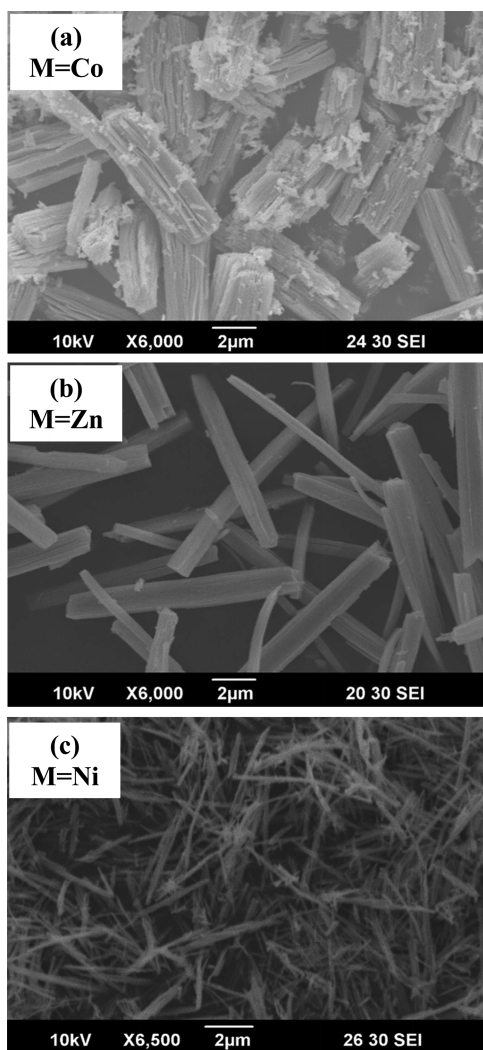
Figure 2. SEM micrographs of the mesoporous MCo_2O_4 rods: (a) M = Co, (b) M = Zn, and (c) M = Ni.

are observed for $NiCo_2O_4$ (Figure 2c). The length of these rods is found to be 5−10 μm for all samples. Figure 3a−f reveals the microstructural features of these samples investigated by TEM. The TEM images (Figure 3a−c) show the agglomerated rods (thickness from few nanometers to few microns) with a length of several micrometers. The SAED patterns (inset of Figure 3d−f) clearly reveal bright spots on the diffraction rings, indicating the nanostructure of the samples. The electron diffraction rings represent the (111), (220), (311), (400), (511), and (440) planes of the spinel structure which is in good agreement with the XRD results. Further, HR-TEM images (Figure 3d−f) also reveal that the rods are built by self-assembled nanoparticle aggregates which are well-interconnected to form stable mesoporous rods. The interplanar distances of MCo_2O_4 mesoporous rods (inset of Figure 3d−f) are found to be 0.245 nm for $CoCo_2O_4$, 0.244 nm for $ZnCo_2O_4$, and 0.245 nm for $NiCo_2O_4$ which matches well with the (311) plane of the spinel structure. The pore size distributions and specific surface area for the MCo_2O_4 rods were evaluated using the BET theory and the BJH model. The N_2 adsorption/desorption isotherms and pore size distribution data for MCo_2O_4 (M = Zn and Ni) are shown in Figure 4. The BET data of $CoCo_2O_4$ are not included for the sake of clarity. The calculated BET specific surface areas of $CoCo_2O_4$, $ZnCo_2O_4$, and $NiCo_2O_4$ were about 24, 54, and 62 m^2 g^{-1}, respectively. The

average pore sizes of $CoCo_2O_4$, $ZnCo_2O_4$, and $NiCo_2O_4$ are 31, 15, and 9 nm, respectively. It clearly reveals the mesoporous structure of the samples. The large surface area can effectively enhance the electrochemical reaction and allow better penetration of the electrolyte for the faradaic reaction.

Raman spectroscopy is used to acquire details about the structural changes, lattice disorder, and compositional changes owing to the divalent cation replacement in the mesoporous cobaltite. Figure 5 shows the Raman spectra of the mesoporous spinel-type rods. Raman active bands at 194, 482, 522, 618, and 690 cm^{-1} corresponding to F_{2g}, E_g, 2F_{2g}, and A_{1g} modes are identified for single-crystal Co_3O_4 by Hadjiev et al.,[32] whereas Raman active vibration peaks at 186, 460, 505, and 659 cm^{-1} corresponding to F_{2g}, E_g, F_{2g}, and A_{1g} modes, respectively, are reported for urchin-like structured $NiCo_2O_4$ by Umeshbabu et al.[33] The shifts in the Raman active mode of urchin-like structured $NiCo_2O_4$ in comparison to those of single-crystal Co_3O_4 were ascribed to Ni substitution for Co and the presence of the nanostructure. In this work, the vibrational peaks of mesoporous $CoCo_2O_4$ rods are observed at 478, 520, 617, and 688 cm^{-1} corresponding to E_g, F_{2g}, F_{2g}, and A_{1g} modes, respectively, which are in agreement with the literature.[34] For $NiCo_2O_4$ rods, the vibration peaks are observed at 475, 516, 613, and 684 cm^{-1} corresponding again to E_g, F_{2g}, F_{2g}, and A_{1g} modes, respectively. Similarly, the vibrational peaks of $ZnCo_2O_4$ rods are observed at 466, 510, 604, and 678 cm^{-1}. The vibrational peaks are shifted toward lower wavenumbers with divalent cation substitution Co > Ni > Zn in the spinel structure. This result further supports the presence of the cubic spinel-type structure for the fabricated mesoporous rods.

The surface elemental composition and the component's oxidation state of the different mesoporous rods were investigated by XPS, and their respective metal 2p spectra are shown in Figure 6. The corresponding main O 1s peaks at 530.3, 529.9, and 529.8 eV are attributed to the spinel lattice oxygen of $CoCo_2O_4$, $ZnCo_2O_4$, and $NiCo_2O_4$, respectively, and are shown in Figure S1 of the Supporting Information together with the C 1s spectra to prove the only weak topmost contamination.[35−37]

For the transition-metal 2p multiplet fitting, we agreed to use only the 2p$_{3/2}$ component of the spin−orbit doublet justified by the sufficient energy gap between both peaks. To address the complex multiplet structure of the third-row transition-metal photoelectron and loss feature multiplets, we follow the approaches of Biesinger and Grosvenor for the interpretation of the Co and Ni multiplets.[38,39] In particular, we used templates of pure Co^{2+} and Co^{3+} 2p multiplets to describe the $CoCo_2O_4$ compound in Figure 6a. Because of the strong overlap of the respective photoelectron peaks, the sole attempt to distinguish between the two binding states is to utilize the respective satellite features around 785.6 eV (Co^{2+}) and 789.7 eV (Co^{3+}) as guiding peaks for the respective multiplets. This is corroborated by the pure Co^{3+} multiplet of $ZnCo_2O_4$ in Figure 6c. The overall Co quantification for $CoCo_2O_4$ finally results in a Co^{3+} amount of 62 at % which is close to the expected content. The Co 2p spectrum of $ZnCo_2O_4$ in Figure 6c reveals, as already stated above, a pure Co^{3+} multiplet justified by the absence of the Co^{2+} satellite. By contrast, the corresponding Zn 2p$_{3/2}$ multiplet in Figure 6d results in two Zn^{2+} components at 1021.4 and 1022.8 eV which indicate Zn^{2+} in tetrahedral and octahedral oxygen coordination, respectively.[40,41] This is supported by the fact that in nanostructured oxide spinels often an almost random arrangement of the different cations on the tetrahedral and octahedral cation sites is observed.[42,43] The chemical state of Zn^{2+} is
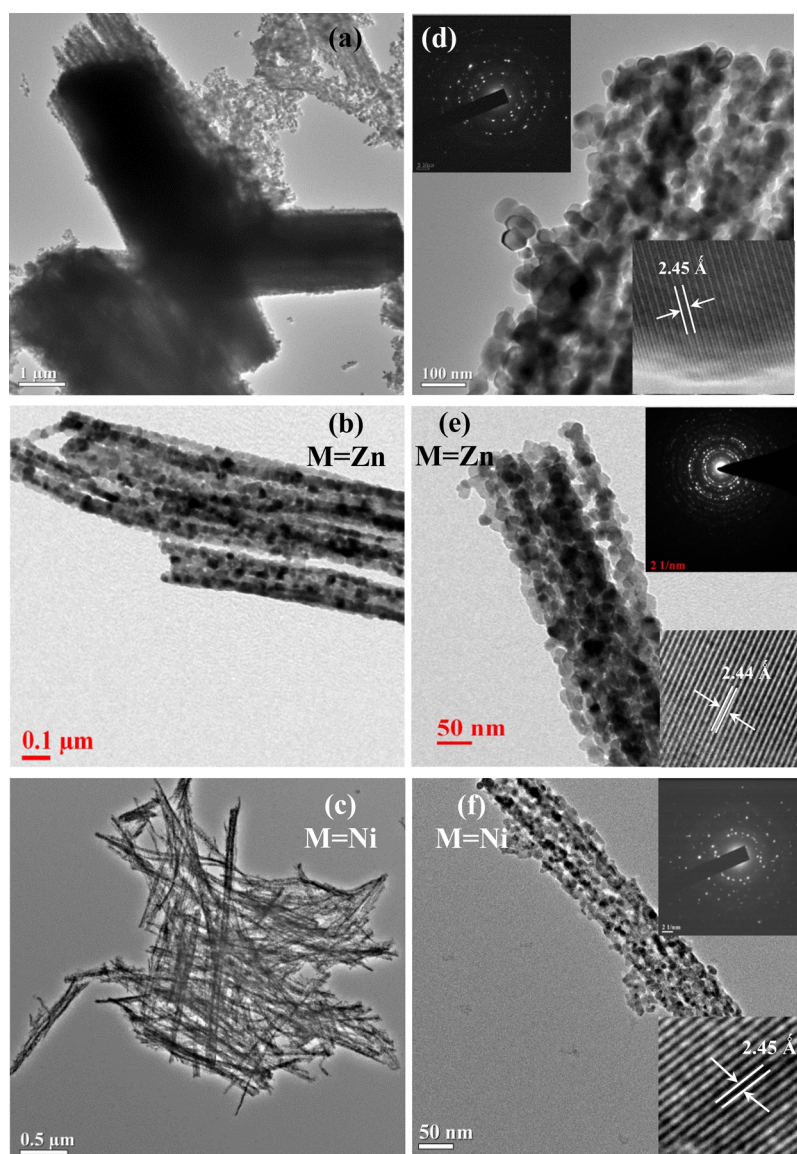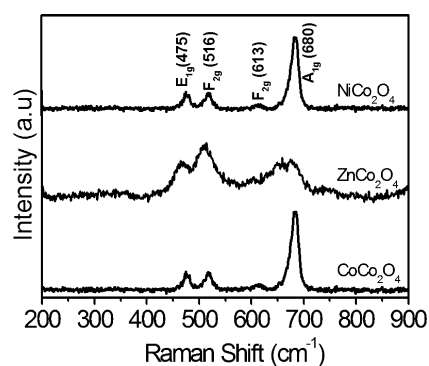
Figure 3. TEM images of the mesoporous MCo_2O_4 rods: (a) M = Co, (b) M = Zn, and (c) M = Ni. High-resolution images of the MCo_2O_4 rods: (d) M = Co, (e) M = Zn, and (f) M = Ni. The inset shows corresponding SEAD pattern and high-resolution lattice image.
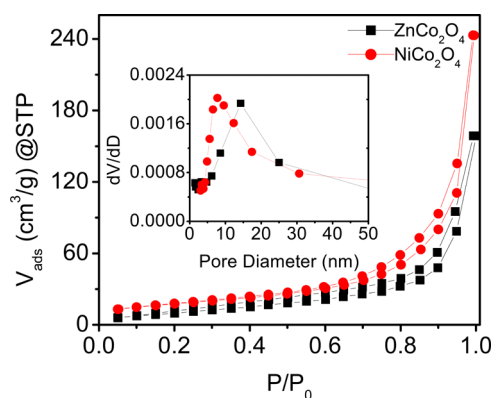
Figure 4. Nitrogen adsorption/desorption isotherm and the corresponding pore size distribution (inset) of the mesoporous MCo_2O_4 rods.

additionally corroborated by the Zn LMM Auger peaks in Figure 6b.

Figure 5. Raman spectra of the mesoporous MCo_2O_4 rods where M = Co, Zn, and Ni.

The Co 2p spectrum of $NiCo_2O_4$ in Figure 6e was fitted according to the procedure described for the $CoCo_2O_4$ compound. In conclusion, we have to consider the presence of a certain amount of Co^{2+} because of the pronounced satellite
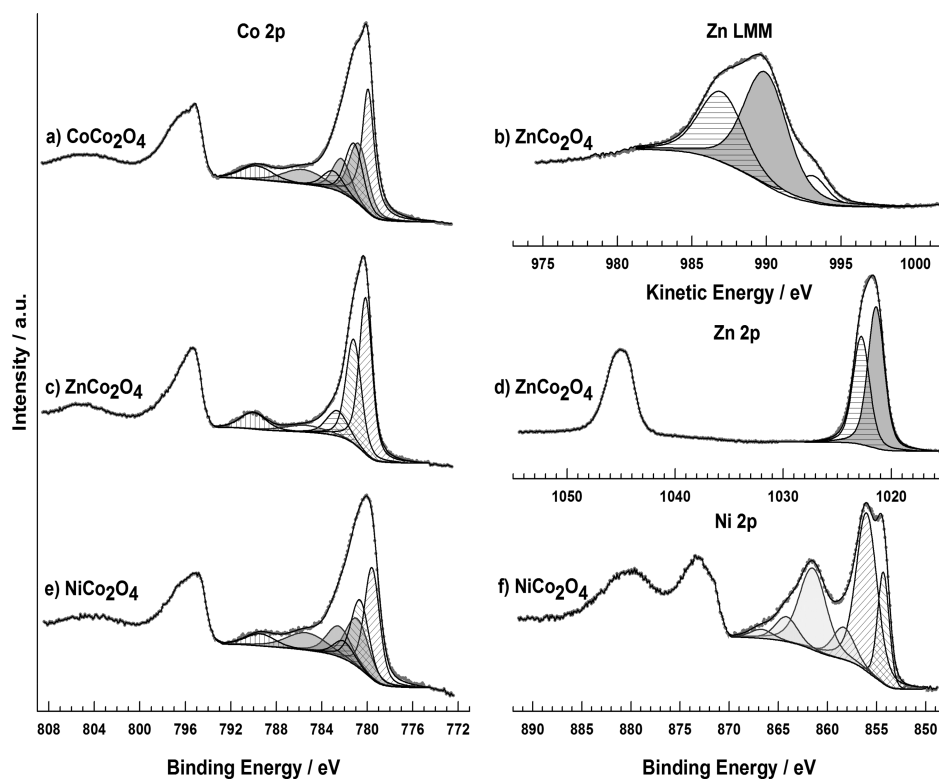
Figure 6. Co 2p, Ni 2p, Zn 2p, and Zn LMM spectra of $CoCo_2O_4$ (a), $ZnCo_2O_4$ (b−d), and $NiCo_2O_4$ (e,f) mesoporous rods. In particular, (a,c,e) Co^{3+} peaks and satellites: shaded and Co^{2+} peaks and satellites: gray; (b,d) Zn^{2+} tetrahedral coordination: gray and octahedral coordination: shaded; and (f) Ni peaks: shaded and loss features: gray.
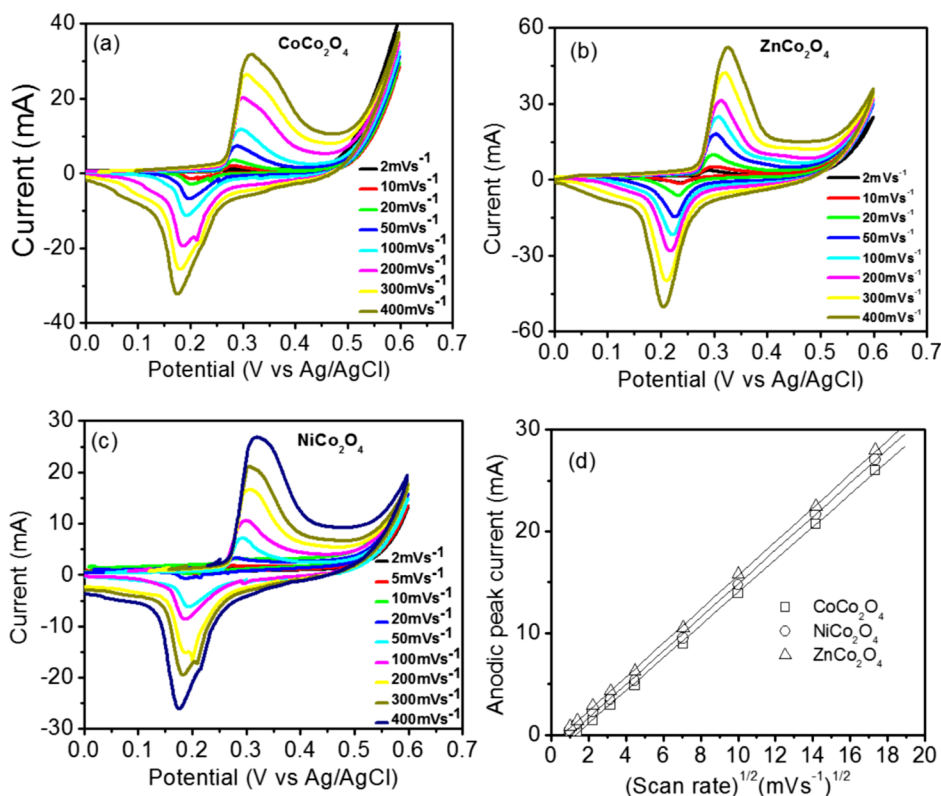
Figure 7. CV of mesoporous rods as a function of scan rate for (a) $CoCo_2O_4$, (b) $ZnCo_2O_4$, and (c) $NiCo_2O_4$. (d) Anodic peak current density against the square root of the scan rate for mesoporous MCo_2O_4 rods.

feature at 785.4 eV. Finally, the Co^{3+} concentration amounts to 59% of the overall Co content. The corresponding Ni 2p

spectrum in Figure 6f was fitted using an adapted template used in the study of Grosvenor et al. and checked by reference
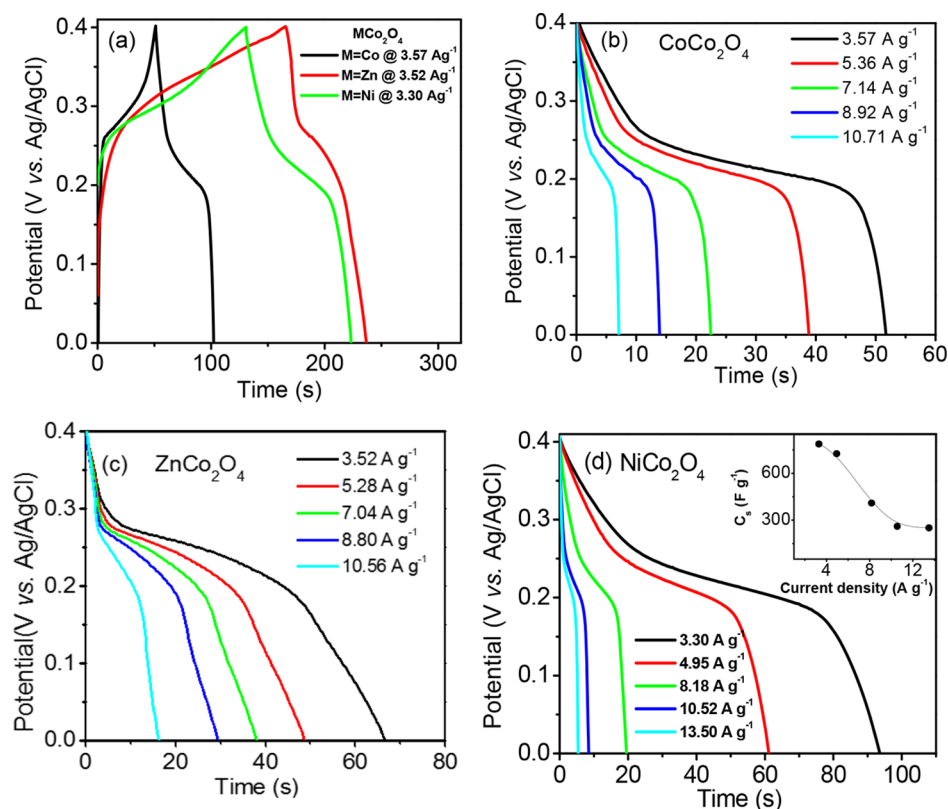
Figure 8. (a) GCD curves of working electrodes (mesoporous MCo_2O_4 rods; M = Co, Zn, and Ni) at a given current density. Discharge curves of mesoporous MCo_2O_4 rods (b) $CoCo_2O_4$, (c) $ZnCo_2O_4$, and (d) $NiCo_2O_4$ at different current densities, and the inset figure shows the specific capacitance vs current density obtained from the discharge curves.

measurements using pure NiO (not shown);[27] as for Ni^{2+} in pure NiO, the ratio between the peaks at 855.9 and at 854.3 eV amounts to 1.5. In the case of the $NiCo_2O_4$ rods, this ratio is about 2.8; hence, in conclusion, a distinct amount of Ni^{3+} has to be considered because the main peak for Ni^{3+} is expected at around 856.0 eV. However, because of the lack of appropriate Ni^{3+} reference materials and, therefore, an unavailable template for the respective multiplet, this cannot be assigned unambiguously. Nevertheless, the assumption seems to be evidenced by the corresponding amount of Co^{2+}, suggesting some Co/Ni exchange. From the results described above, the following conclusions can be drawn: (i) The Co^{3+} content of 62% found for $CoCo_2O_4$ is to some extent smaller than 2/3 and might hint at some oxygen deficiency. (ii) $NiCo_2O_4$ shows mixed valences for both the transition-metal elements which compensate each other. (iii) $ZnCo_2O_4$ shows site exchange for Zn and Co, that is, a partially inverse spinel. The Co^{2+}/Co^{3+} and Ni^{2+}/Ni^{3+} redox couples are the major active sites for the electrochemical reactions.

The CV of MCo_2O_4 (M = Co, Zn, and Ni) mesoporous rods with 6 M KOH as the electrolyte is performed to evaluate the pseudocapacitor performance. Figure 7a−c shows the CV curves for the MCo_2O_4 mesoporous rods in a potential window of 0.0–0.6 V versus Ag/AgCl at different scan rates. The well-defined oxidation and reduction peaks are observed in the cathodic and anodic scans in all CV curves, revealing that the capacitance of the mesoporous spinel-type metal oxide working electrodes is primarily based on the redox reaction.[16] All CV curves show an almost identical shape, and the redox current increases with the scan rate. The peaks in the CV are ascribed to the electrochemical redox reactions associated with M−O/M−O−OH (M = Co, Zn,

and Ni).[44] The most probable electrochemical redox reactions can be described for the present mesoporous rods in the alkaline electrolyte solution as

$$MCo_2O_4 + OH^- + H_2O \leftrightarrow MOOH + 2CoOOH + e^- \tag{1}$$

$$CoOOH + OH^- \leftrightarrow CoO_2 + H_2O + e^- \tag{2}$$
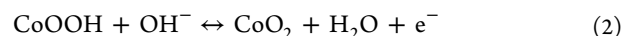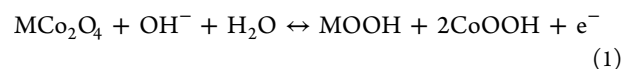
With increasing scan rate, the anodic and cathodic peak position is shifted toward higher and lower potentials, respectively, which indicates the faradaic reaction.[12] The charge stored in the mesoporous electrode is given by the area enclosed by the CV curve. The Coulombic efficiency (η) is represented as the ratio between the area of oxidation and reduction peaks. The η of mesoporous MCo_2O_4 rods, where M = Co, Zn, and Ni, estimated from the CV curves at 5 mV/s (scan rate) is 95.23%. The η is enhanced up to 97.78% for a scan rate of 100 mV/s. The specific capacitance (C_s) of the mesoporous rods is determined from the CV data by using the following equation[9]

$$C_s = \frac{1}{2m\nu(E_2 - E_1)} \int_{E_1}^{E_2} i(E)\,dE \tag{3}$$

where m is the mass of the active material, ν is the scan rate, ($E_2 - E_1$) is the potential window, and $i(E)$ is the current at each potential. The C_s values of these mesoporous rods are found to be 1846 F g^{-1} for $CoCo_2O_4$, 1983 F g^{-1} for $ZnCo_2O_4$, and 2118 F g^{-1} for $NiCo_2O_4$ at a scan rate of 2 mV/s. The C_s values decrease to 1665 F g^{-1} for $CoCo_2O_4$, 1738 F g^{-1} for $ZnCo_2O_4$, and 1911 F g^{-1} for $NiCo_2O_4$ at a scan rate of 50 mV/s. It reveals that ion diffusion is restricted in the surface of the active materials at higher scan rate. Thus, the electric double layer capacitance

dominates over the pseudocapacitance at higher scan rate. The faradaic reaction dominates at low scan rates (<10 mV/s) which leads to the enhancement of the specific capacitance because of the more effective usage of the active material in the working electrode. The diffusion of OH$^-$ ions is the rate-controlling process which is confirmed by observing a linear relation between the anodic peak current and the square root of the scan rate, as shown in Figure 7d. Among these mesoporous MCo$_2$O$_4$ rods (M = Co, Zn, and Ni), NiCo$_2$O$_4$ shows the highest specific capacitance because of larger surface area with smaller pore size.

To further investigate the specific capacitance of these samples, GCD experiments were performed. Figure 8a shows the GCD curves of the working electrodes at a given current density. The asymmetric shape of the GCD curves represents the faradaic nature of the materials. The CoCo$_2$O$_4$ electrode is quickly charged to 0.4 V at 3.57 A g^{-1} in comparison with the charging time of ZnCo$_2$O$_4$ (3.52 A g^{-1}) and NiCo$_2$O$_4$ (3.30 A g^{-1}) electrodes (51, 160, and 130 s for M = Co, Zn, and Ni, respectively). According to the BJH study, the pore size of the CoCo$_2$O$_4$ rods is higher than that of the other two samples and it facilitates ion movements into the electrode for the electrochemical reaction or screening of the external electric field. While comparing the discharge time of the electrodes (53, 71, and 94 s for M = Co, Zn, and Ni, respectively), the NiCo$_2$O$_4$ electrode shows the higher discharge capacity because of the larger surface area in comparison to the other two electrodes. This large surface area of the electrode allows to store more charge or to access more active sites for the redox reaction.

To determine the practical specific capacitance of these electrodes, the charge/discharge measurements at different current densities were carried out, as shown in Figure 8b−d. All discharge curves exhibit three different regimes: (i) initially, a rapid potential drop occurs owing to internal resistance, (ii) a slow potential decay at intermediate times caused by the faradaic redox reaction, and (iii) finally, a fast potential decay owing to the electric double layer capacitance. C_s is estimated from the discharge curves by using the following expression[9]

$$C_s = \frac{I \times \Delta t}{m \times \Delta v} \qquad (4)$$

where I, Δt, m, and Δv are the applied current, discharge time, active mass, and potential difference, respectively. The C_s values of CoCo$_2$O$_4$, ZnCo$_2$O$_4$, and NiCo$_2$O$_4$ are 473 F g^{-1} at 3.57 A g^{-1}, 590 F g^{-1} at 3.52 A g^{-1}, and 788 F g^{-1} at 3.30 A g^{-1}, respectively. The C_s of NiCo$_2$O$_4$ decreases with the current density, as shown in the inset of Figure 8d, and similar features are observed for the other samples too. The C_s of the NiCo$_2$O$_4$ electrode is superior in comparison with that of the other two electrodes. Considering the BET and HR-TEM results, the larger surface area and highly porous nature of NiCo$_2$O$_4$ are anticipated to result in the higher C_s. A good cycling stability is vital for real capacitor applications. Therefore, we have carried out continuous GCD measurement for about 2000 cycles, as shown in Figure 9. A few continuous GCD cycles for NiCo$_2$O$_4$ at a current density of 3.30 A g^{-1} is shown in the inset of Figure 9. After 2000 cycles, the MCo$_2$O$_4$ electrodes where M = Co, Zn, and Ni are maintained at 94.93, 95.94, and 97.11% of their initial C_s, respectively. It reveals that the mesoporous spinel-type metal oxide rods show the desirable stability in the 6 M KOH electrolyte during long-term cycling with excellent cycling efficiency. In Table 1, we summarized the C_s values of the samples from the present work in comparison with the C_s of 1D MCo$_2$O$_4$ where M = Co, Zn, and Ni obtained by the template route in the literature.[24,45−48] The C_s value of the
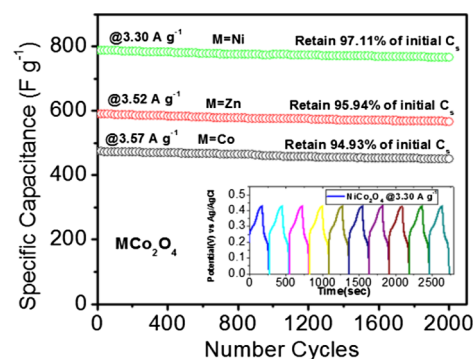

Figure 9. Cycle performance of mesoporous MCo$_2$O$_4$ rods; M = Co, Zn, and Ni at a given density. The inset shows the continuous GCD cycle for NiCo$_2$O$_4$ at 3.30 A g^{-1}.

Table 1. Specific Capacitance (C_s) of the Samples from the Present Work in Comparison with the C_s of 1D MCo$_2$O$_4$ Where M = Co, Zn, and Ni Obtained by the Template Route in the Literature

materials	synthesized by template route	C_s (F g^{-1})	current density/sweep rate	references
CoCo$_2$O$_4$ nanorods	CTAB as a template	456	1 A g^{-1}	45
CoCo$_2$O$_4$ nanowires	SBA-15 as a template	373	3 mV/s	46
CoCo$_2$O$_4$ nanorods	H3BTC as a template	262	5 mV/s	47
CoCo$_2$O$_4$ nanorods	SBA-15 as a template	253	0.5 A g^{-1}	48
CoCo$_2$O$_4$ nanorods	KIT-6 as a template	370	0.5 A g^{-1}	48
CoCo$_2$O$_4$ nanofibers	P123 as a template	401	5 A g^{-1}	49
CoCo$_2$O$_4$ mesoporous rods	template free	473	3.57 A g^{-1}	present work
CoCo$_2$O$_4$ mesoporous rods	template free	1846	2 mV/s	present work
ZnCo$_2$O$_4$ rods	PVP as a template	382	3 A g^{-1}	24
ZnCo$_2$O$_4$ nanoneedle	P123 as a template	367	2 mV/s	50
ZnCo$_2$O$_4$ porous rods	template-free route	590	3.52 A g^{-1}	present work
ZnCo$_2$O$_4$ porous rods	template-free route	1983	2 mV/s	present work
NiCo$_2$O$_4$ nanofibers	cotton fibers as templates	981	1 A g^{-1}	51
NiCo$_2$O$_4$ nanowires	P123 as a template	743	1 A g^{-1}	52
NiCo$_2$O$_4$ nanowires	P123 as a template	722	1 A g^{-1}	53
NiCo$_2$O$_4$ nanofibers	PVP as a template	987	1 A g^{-1}	54
NiCo$_2$O$_4$ porous rods	template-free route	788	3.30 A g^{-1}	present work
NiCo$_2$O$_4$ porous rods	template-free route	2118	2 mV/s	present work

present work is superior to some pioneering 1D MCo$_2$O$_4$ electrodes obtained by template routes. In particular, the porous nanorods are built by the aggregates of nanoparticles, and thus, the electrolyte can easily penetrate through the porous 1D structure which helps for efficient redox reactions during the faradaic charge storage mechanism. Hence, the majority of the
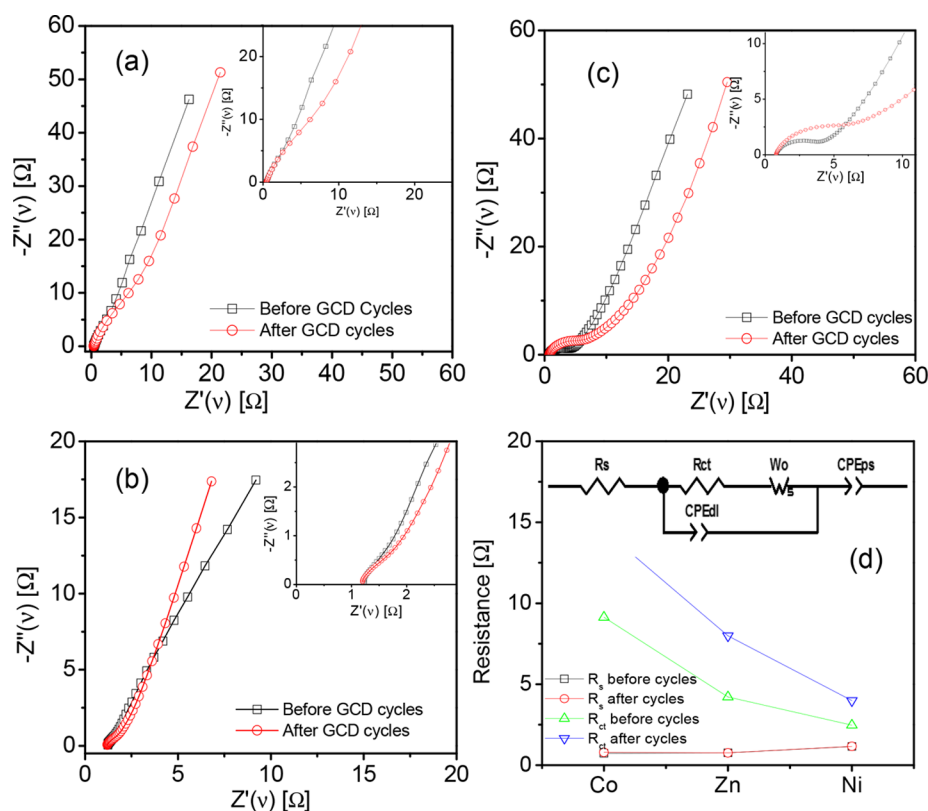
Figure 10. Complex impedance spectra of mesoporous MCo_2O_4 rods in 6 M KOH solution before and after 2000 cycles test for (a) $CoCo_2O_4$, (b) $ZnCo_2O_4$, and (c) $NiCo_2O_4$. (d) Resistance R_s and R_{ct} of mesoporous MCo_2O_4 rods before and after 2000 cycles test. The inset of the figure shows a representative EC.

electroactive sites of the 1D porous MCo_2O_4 electrodes are utilized efficiently, resulting in higher specific capacitance with better cycling efficiency.

The electrochemical impedance spectroscopic (EIS) measurements were carried out before and after GCD cycles to investigate the charge-transfer reaction mechanism of the electrodes. Figure 10a−c shows the complex impedance plots of working electrodes before and after 2000 cycles at a given current density. The following features are observed in the complex impedance spectra. An offset in the real part of impedance (R_s) at high frequencies represents a sum of intrinsic resistance of the active material, contact resistance, and electrolyte resistance. A small semicircle is observed at high to intermediate frequencies. It represents the faradaic charge-transfer resistance (R_{ct}) of the electrochemical reactions between the electrode and the electrolyte. A straight line is observed in the low-frequency region which originates from the diffusive resistance of anions (OH^-) from the liquid electrolyte to the solid oxide electrode surface. To quantify the bulk resistance and faradaic charge-transfer resistance of the electrodes before and after the GCD cycles, the EIS data were analyzed with electrical equivalent circuits (ECs) using ZView (version 2.70) software. A representative EC is shown in the inset of Figure 10d. In the EC, R_s, R_{ct}, W, CPE_{dl}, and CPE_{ps} refer to the bulk resistance, faradaic charge-transfer resistance, Warburg impedance, constant phase element of double layer capacitance, and pseudocapacitance, respectively. All electrodes show almost the same bulk resistance before and after the GCD cycles, as shown in Figure 10d. However, the bulk resistance of the $NiCo_2O_4$ electrode is slightly higher than that of the other two electrodes (Figure 10d). It might be caused by a larger grain boundary resistance between

grains as expected because of the smaller grain sizes. The charge-transfer resistance of the $CoCo_2O_4$ and $ZnCo_2O_4$ electrodes increased after the GCD cycling, indicating that the fading of the faradaic electrochemical reaction may result from the formation of inactive sites or a loss of adhesion of some active material to the current collector. The resistance R_{ct} of the $NiCo_2O_4$ electrode increased slightly after cycling. This could be the major benefit of this electrode which possesses a highly porous structure that leads to fast ion/electron transfers at the electrode/electrolyte interface.

3. CONCLUSIONS

The spinel-type MCo_2O_4 (M = Co, Zn, and Ni) mesoporous rods were successfully synthesized by a simple solvothermal route without surfactants and a post-annealing approach. The length of these mesoporous rods is found to be of several micrometers. The XRD measurements reveal a phase-pure spinel-type crystal structure with lattice parameters of a = 8.118, 8.106, and 8.125 Å for MCo_2O_4, M = Co, Zn, and Ni, respectively. The HR-TEM study reveals that the mesoporous rods are built by self-assembled nanoparticle aggregates which are well-interconnected to form stable mesoporous rods. The spinel-type MCo_2O_4 rods exhibit high specific capacitances of 1846 F g^{-1} ($CoCo_2O_4$), 1983 F g^{-1} ($ZnCo_2O_4$), and 2118 F g^{-1} ($NiCo_2O_4$) at a scan rate of 2 mV/s. The mesoporous MCo_2O_4, M = Co, Zn, and Ni, rods show an excellent cycling stability with 94.93% at 3.57 A g^{-1}, 95.94% at 3.52 A g^{-1}, and 97.11% at 3.30 A g^{-1}, respectively, of their initial C_s even after 2000 cycles. The mesoporous spinel-type metal oxides reveal the desirable stability in the alkaline electrolyte during long-term cycling with excellent cycling efficiency.

4. MATERIALS AND METHODS

The spinel-type MCo_2O_4 (M = Co, Zn, and Ni) mesoporous rods were fabricated by a simple solvothermal approach without the assistance of surfactants. The $NiCo_2O_4$ mesoporous rods were prepared by mixing 1 mmol $Ni(SO_4)_2 \cdot 7H_2O$ (Loba Chemie) and 2 mmol $CoSO_4 \cdot 7H_2O$ (Loba Chemie) and dissolving this mixture in EG and deionized water (3:1 v/v ratio) under magnetic stirring. $H_2C_2O_4$ (3 mmol, Loba Chemie) was added to this solution slowly under continuous stirring for about 1 h at room temperature (RT). The final mixture was poured into an autoclave (Teflon-lined stainless steel) with a volume of 100 mL and hydrothermally treated at 140 °C for 24 h in an oven. The products were collected by centrifugation, washed with deionized water several times, and dried in air at 80 °C for 10 h. The $ZnCo_2O_4$ rods were prepared by mixing 2 mmol $CoSO_4 \cdot 7H_2O$ and 1 mmol $Zn(SO_4)_2 \cdot 7H_2O$ (Loba Chemie), and the Co_3O_4 mesoporous rods were synthesized by taking 3 mmol $CoSO_4 \cdot 7H_2O$, while the other steps were identical to those of the $NiCo_2O_4$ rods. Finally, the product precursors were heated at 450 °C for 2 h with a heating rate of 5 °C min^{-1} and cooled down slowly to RT.

The powder XRD data of the samples were acquired with a MiniFlex-II (Rigaku) diffractometer with λ_{Cu} = 1.541 Å operating at a voltage of 40 kV and a current of 30 mA. The TGA−DTA were performed using a simultaneous thermal analyzer (Hitachi, STA7000 series) at temperatures from 30 to 1000 °C at a heating rate of 5 °C min^{-1} in air. The microstructural properties were analyzed by SEM (JEOL JSM-6390LV) and TEM (Tecnai G^{2}20 S-Twin and Jeol JEM 2100) with SAED. The specific surface area and pore size distributions were evaluated according to the BET theory and BJH model, respectively (Quantachrome, QUAD-RASORB SI). The Raman spectra were measured with a Renishaw laser Raman spectrometer.

The XPS measurements were performed using a K-Alpha XPS + instrument (Thermo Fisher Scientific, East Grinstead, UK). Data acquisition and processing using the Thermo Avantage software is described elsewhere.[27] The mesoporous rods were analyzed using a microfocused, monochromated Al Kα X-ray source with 30−400 μm spot size. The K-Alpha charge compensation system was employed during the analysis, using electrons of 8 eV energy and low-energy argon ions to prevent any localized charge build-up. The spectra were fitted with one or more Voigt profiles. All spectra were referenced to the C 1s peak of hydrocarbon at a 285.0 eV binding energy controlled by means of the well-known photoelectron peaks of metallic Cu, Ag, and Au. For intense peaks and/or peaks clearly evidenced by the peak shape, the binding energy uncertainty was around ±0.1 eV. In the case of weak peaks and no direct justification by the peak shape, the uncertainty was set to ±0.2 eV. The analyzer transmission function, Scofield's sensitivity factors,[28] and effective attenuation lengths (EALs) for photoelectrons were applied for quantification. The EALs were calculated using the standard TPP-2M formalism.[29]

The electrode slurry was prepared by mixing the MCo_2O_4 (M = Co, Zn, and Ni) mesoporous rods (80 wt %), activated charcoal carbon black (SD FINE-CHEM, 10 wt %), polyvinylidene fluoride (Alfa Aesar, 10 wt %) with N-methyl pyrrolidinone (Loba Chemie) as a solvent. Initially, the Ni mesh (Alfa Aesar) substrate was cleaned by ultrasonication. Then, the slurry of the electrode materials was pasted on the cleaned Ni mesh substrate as a working electrode, and it was dried at 80 °C for 24 h. Finally, the working electrode was compacted with a hydraulic press (load of 5 t). The working electrode area was 1 cm^2 (geometrical area) with an active electrode mass of ∼1 mg. The electrochemical performance was investigated by CV, GCD cycling, and impedance spectroscopy in a three-electrode configuration. KOH (6 M) was used as an electrolyte. A potentiostat/galvanostat (Biologic, SP-240) was used for the electrochemical measurements with EC lab software. Ag/AgCl was used as a reference electrode and a platinum rod was used as a counter electrode.

■ ASSOCIATED CONTENT

⑤ Supporting Information

The Supporting Information is available free of charge on the ACS Publications website at DOI: 10.1021/acsomega.7b00709.

O 1s and C 1s XP spectra of $CoCo_2O_4$, $ZnCo_2O_4$, and $NiCo_2O_4$ mesoporous rods (PDF)

■ AUTHOR INFORMATION

Corresponding Author

*E-mail: crmari2005@yahoo.com. Phone: +91-1744-233-498. Fax: +91-1744-238-050 (C.R.M.).

ORCID 🄭

Chinnasamy Ramaraj Mariappan: 0000-0002-8255-962X

Sylvio Indris: 0000-0002-5100-113X

Notes

The authors declare no competing financial interest.

■ REFERENCES

(1) Melot, B. C.; Tarascon, J.-M. Design and Preparation of Materials for Advanced Electrochemical Storage. *Acc. Chem. Res.* **2013**, *46*, 1226−1238.

(2) Miller, J. R.; Simon, P. Electrochemical Capacitors for Energy Management. *Science* **2008**, *321*, 651−652.

(3) Choi, N.-S.; Chen, Z.; Freunberger, S. A.; Ji, X.; Sun, Y.-K.; Amine, K.; Yushin, G.; Nazar, L. F.; Cho, J.; Bruce, P. G. Challenges Facing Lithium Batteries and Electrical Double-Layer Capacitors. *Angew. Chem., Int. Ed.* **2012**, *51*, 9994−10024.

(4) El-Kady, M. F.; Shao, Y.; Kaner, R. B. Graphene for Batteries, Supercapacitors and Beyond. *Nat. Rev. Mater.* **2016**, *1*, 16033.

(5) Yang, Z.; Zhang, J.; Kintner-Meyer, M. C. W.; Lu, X.; Choi, D.; Lemmon, J. P.; Liu, J. Electrochemical Energy Storage for Green Grid. *Chem. Rev.* **2011**, *111*, 3577−3613.

(6) Simon, P.; Gogotsi, Y.; Dunn, B. Where do Batteries End and Supercapacitors Begin? *Science* **2014**, *343*, 1210−1211.

(7) Kim, H.-S.; Cook, J. B.; Lin, H.; Ko, J. S.; Tolbert, S. H.; Ozolins, V.; Dunn, B. Oxygen Vacancies Enhance Pseudocapacitive Charge Storage Properties of $MoO_{3−x}$. *Nat. Mater.* **2017**, *16*, 454−460.

(8) Augustyn, V.; Simon, P.; Dunn, B. Pseudocapacitive Oxide Materials for High-rate Electrochemical Energy Storage. *Energy Environ. Sci.* **2014**, *7*, 1597−1614.

(9) Wang, G.; Zhang, L.; Zhang, J. A Review of Electrode Materials for Electrochemical Supercapacitors. *Chem. Soc. Rev.* **2012**, *41*, 797−828.

(10) Sugimoto, W.; Iwata, H.; Yasunaga, Y.; Murakami, Y.; Takasu, Y. Preparation of Ruthenic Acid Nanosheets and Utilization of Its

Interlayer Surface for Electrochemical Energy Storage. *Angew. Chem., Int. Ed.* **2003**, *42*, 4092−4096.

(11) Zheng, J. P.; Cygan, P. J.; Jow, T. R. Hydrous Ruthenium Oxide as an Electrode Material for Electrochemical Capacitors. *J. Electrochem. Soc.* **1995**, *142*, 2699.

(12) Wang, H.; Gao, Q.; Jiang, L. Facile Approach to Prepare Nickel Cobaltite Nanowire Materials for Supercapacitors. *Small* **2011**, *7*, 2454−2459.

(13) Park, M.-S.; Kim, J.; Kim, K. J.; Lee, J.-W.; Kim, J. H.; Yamauchi, Y. Porous Nanoarchitectures of Spinel-type Transition Metal Oxides for Electrochemical Energy Storage Systems. *Phys. Chem. Chem. Phys.* **2015**, *17*, 30963−30977.

(14) Zhang, Y.; Li, L.; Su, H.; Huang, W.; Dong, X. Binary Metal Oxide: Advanced Energy Storage Materials in Supercapacitors. *J. Mater. Chem. A* **2015**, *3*, 43−59.

(15) Xiong, S.; Yuan, C.; Zhang, X.; Xi, B.; Qian, Y. Controllable Synthesis of Mesoporous Co_3O_4 Nanostructures with Tunable Morphology for Application in Supercapacitors. *Chem.—Eur. J.* **2009**, *15*, 5320−5326.

(16) Pendashteh, A.; Rahmanifar, M. S.; Kaner, R. B.; Mousavi, M. F. Facile Synthesis of Nanostructured $CuCo_2O_4$ as a Novel Electrode Material for High-rate Supercapacitors. *Chem. Commun.* **2014**, *50*, 1972−1975.

(17) Krishnan, S. G.; Reddy, M. V.; Harilal, M.; Vidyadharan, B.; Misnon, I. I.; Rahim, M. H. A.; Ismail, J.; Jose, R. Characterization of $MgCo_2O_4$ as an Electrode for High Performance Supercapacitors. *Electrochim. Acta* **2015**, *161*, 312−321.

(18) Zhou, G.; Zhu, J.; Chen, Y.; Mei, L.; Duan, X.; Zhang, G.; Chen, L.; Wang, T.; Lu, B. Simple Method for the Preparation of Highly Porous $ZnCo_2O_4$ Nanotubes with Enhanced Electrochemical Property for Supercapacitor. *Electrochim. Acta* **2014**, *123*, 450−455.

(19) Wu, H.; Lou, Z.; Yang, H.; Shen, G. A Flexible Spiral-type Supercapacitor Based on $ZnCo_2O_4$ Nanorod Electrodes. *Nanoscale* **2015**, *7*, 1921−1926.

(20) Zhang, Y.; Ma, M.; Yang, J.; Su, H.; Huang, W.; Dong, X. Selective Synthesis of Hierarchical Mesoporous Spinel $NiCo_2O_4$ for High-performance Supercapacitors. *Nanoscale* **2014**, *6*, 4303−4308.

(21) Du, J.; Zhou, G.; Zhang, H.; Cheng, C.; Ma, J.; Wei, W.; Chen, L.; Wang, T. Ultrathin Porous $NiCo_2O_4$ Nanosheet Arrays on Flexible Carbon Fabric for High-Performance Supercapacitors. *ACS Appl. Mater. Interfaces* **2013**, *5*, 7405−7409.

(22) Yuan, C.; Li, J.; Hou, L.; Zhang, X.; Shen, L.; Lou, X. W. Ultrathin Mesoporous $NiCo_2O_4$ Nanosheets Supported on Ni Foam as Advanced Electrodes for Supercapacitors. *Adv. Funct. Mater.* **2012**, *22*, 4592−4597.

(23) Wang, H.; Wang, X. Growing Nickel Cobaltite Nanowires and Nanosheets on Carbon Cloth with Different Pseudocapacitive Performance. *ACS Appl. Mater. Interfaces* **2013**, *5*, 6255−6260.

(24) Tomboc, G. M.; Jadhav, H. S.; Kim, H. PVP Assisted Morphology-Controlled Synthesis of Hierarchical Mesoporous $ZnCo_2O_4$ Nanoparticles for High-Performance Pseudocapacitor. *Chem. Eng. J.* **2017**, *308*, 202−213.

(25) Ren, B.; Fan, M.; Wang, J.; Jing, X.; Bai, X. The Effect of Pluronic P123 on the Capacitive Behavior of Co_3O_4 as a Self-Assembeled Additive. *J. Electrochem. Soc.* **2013**, *160*, E79−E83.

(26) Yuan, C.; Li, J.; Hou, L.; Lin, J.; Pang, G.; Zhang, L.; Lian, L.; Zhang, X. Template-Engaged Synthesis of Uniform Mesoporous Hollow $NiCo_2O_4$ Sub-Microspheres Towards High-Performance Electrochemical Capacitors. *RSC Adv.* **2013**, *3*, 18573−18578.

(27) Parry, K. L.; Shard, A. G.; Short, R. D.; White, R. G.; Whittle, J. D.; Wright, A. ARXPS Characterisation of Plasma Polymerised Surface Chemical Gradients. *Surf. Interface Anal.* **2006**, *38*, 1497−1504.

(28) Scofield, J. H. Hartree-Slater Subshell Photoionization Cross-Sections at 1254 and 1487 eV. *J. Electron Spectrosc. Relat. Phenom.* **1976**, *8*, 129−137.

(29) Tanuma, S.; Powell, C. J.; Penn, D. R. Calculations of Electron Inelastic Mean Free Paths. V. Data for 14 Organic Compounds Over the 50−2000 eV Range. *Surf. Interface Anal.* **1994**, *21*, 165−176.

(30) Cao, A.-M.; Hu, J.-S.; Liang, H.-P.; Wan, L.-J. Self-Assembled Vanadium Pentoxide (V_2O_5) Hollow Microspheres from Nanorods and

their Application in Lithium-ion Batteries. *Angew. Chem., Int. Ed.* **2005**, *44*, 4391−4395.

(31) Cullity, B. D. *Elements of X-ray Diffraction*; Addison-Wesley Publishing Company Inc.: USA, 1956; pp 259−262.

(32) Hadjiev, V. G.; Iliev, M. N.; Vergilov, I. V. The Raman Spectra of Co_3O_4. *J. Phys. C: Solid State Phys.* **1988**, *21*, L199−L201.

(33) Umeshbabu, E.; Rajeshkhanna, G.; Justin, P.; Rao, G. R. Magnetic, Optical and Electrocatalytic Properties of Urchin and Sheaf-like $NiCo_2O_4$ Nanostructures. *Mater. Chem. Phys.* **2015**, *165*, 235−244.

(34) Wang, G.; Shen, X.; Horvat, J.; Wang, B.; Liu, H.; Wexler, D.; Yao, J. Hydrothermal Synthesis and Optical, Magnetic, and Supercapacitance Properties of Nanoporous Cobalt Oxide Nanorods. *J. Phys. Chem. C* **2009**, *113*, 4357−4361.

(35) Zydziak, N.; Hübner, C.; Bruns, M.; Barner-Kowollik, C. One-Step Functionalization of Single-Walled Carbon Nanotubes (SWCNTs) with Cyclopentadienyl-Capped Macromolecules via Diels−Alder Chemistry. *Macromolecules* **2011**, *44*, 3374−3380.

(36) Baggetto, L.; Unocic, R. R.; Dudney, N. J.; Veith, G. M. Fabrication and Characterization of Li−Mn−Ni−O Sputtered Thin Film High Voltage Cathodes for Li-ion Batteries. *J. Power Sources* **2012**, *211*, 108−118.

(37) Cherkashinin, G.; Nikolowski, K.; Ehrenberg, H.; Jacke, S.; Dimesso, L.; Jaegermann, W. The Stability of the SEI Layer, Surface Composition and the Oxidation State of Transition Metals at the Electrolyte−Cathode Interface Impacted by the Electrochemical Cycling: X-Ray Photoelectron Spectroscopy Investigation. *Phys. Chem. Chem. Phys.* **2012**, *14*, 12321−12331.

(38) Biesinger, M. C.; Payne, B. P.; Grosvenor, A. P.; Lau, L. W. M.; Gerson, A. R.; Smart, R. S. C. Resolving Surface Chemical States in XPS Analysis of First Row Transition Metals, Oxides and Hydroxides: Cr, Mn, Fe, Co and Ni. *Appl. Surf. Sci.* **2001**, *257*, 2717−2730.

(39) Grosvenor, A. P.; Biesinger, M. C.; Smart, R. S. C.; McIntyre, N. S. New Interpretations of XPS Spectra of Nickel Metal and Oxides. *Surf. Sci.* **2006**, *600*, 1771−1779.

(40) Šepelák, V.; Becker, S. M.; Bergmann, I.; Indris, S.; Scheuermann, M.; Feldhoff, A.; Kübel, C.; Bruns, M.; Stürzl, N.; Ulrich, A. S.; Ghafari, M.; Hahn, H.; Grey, C. P.; Becker, K. D.; Heitjans, P. Nonequilibrium Structure of Zn_2SnO_4 Spinel Nanoparticles. *J. Mater. Chem.* **2012**, *22*, 3117−3126.

(41) Šepelák, V.; Indris, S.; Heitjans, P.; Becker, K. D. Direct Determination of the Cation Disorder in Nanoscale Spinels by NMR, XPS, and Mössbauer Spectroscopy. *J. Alloys Compd.* **2007**, *434−435*, 776−778.

(42) Šepelák, V.; Bergmann, I.; Indris, S.; Feldhoff, A.; Hahn, H.; Becker, K. D.; Grey, C. P.; Heitjans, P. High-Resolution 27Al MAS NMR Spectroscopic Studies of the Response of Spinel Aluminates to Mechanical Action. *J. Mater. Chem.* **2011**, *21*, 8332−8337.

(43) Permien, S.; Hain, H.; Scheuermann, M.; Mangold, S.; Mereacre, V.; Powell, A. K.; Indris, S.; Schürmann, U.; Kienle, L.; Duppel, V.; Harm, S.; Bensch, W. Electrochemical Insertion of Li into Nanocrystalline $MnFe_2O_4$: A Study of the Reaction Mechanism. *RSC Adv.* **2013**, *3*, 23001−23014.

(44) Zhou, W.; Kong, D.; Jia, X.; Ding, C.; Cheng, C.; Wen, G. $NiCo_2O_4$ Nanosheet Supported Hierarchical Core−Shell Arrays for High-Performance Supercapacitors. *J. Mater. Chem. A* **2014**, *2*, 6310−6315.

(45) Cui, L.; Li, J.; Zhang, X.-G. Preparation and Properties of Co_3O_4 Nanorods as Supercapacitor Material. *J. Appl. Electrochem.* **2009**, *39*, 1871−1876.

(46) Wang, L.; Liu, X.; Wang, X.; Yang, X.; Lu, L. Electrochemical Capacitance Study on Co_3O_4 Nanowires for Super capacitors Application. *J. Mater. Sci.: Mater. Electron.* **2011**, *22*, 601−606.

(47) Meng, T.; Xu, Q.-Q.; Wang, Z.-H.; Li, Y.-T.; Gao, Z.-M.; Xing, X.-Y.; Ren, T.-Z. Co_3O_4 Nanorods with Self-assembled Nanoparticles in Queue for Supercapacitor. *Electrochim. Acta* **2015**, *180*, 104−111.

(48) Zheng, M.-b.; Cao, J.; Liao, S.-t.; Liu, J.-s.; Chen, H.-q.; Zhao, Y.; Dai, W.-j.; Ji, G.-b.; Cao, J.-m.; Tao, J. Preparation of mesoporous Co_3O_4 nanoparticles via solid−liquid route and effects of calcination temper-

ature and textural parameters on their electrochemical capacitive behaviors. *J. Phys. Chem. C* **2009**, *113*, 3887−3894.

(49) Ren, B.; Fan, M.; Wang, J.; Jing, X.; Bai, X. The Effect of Pluronic P123 on the Capacitive Behavior of Co_3O_4 as a Self-Assembeled Additive. *J. Electrochem. Soc.* **2013**, *160*, E79−E83.

(50) Niu, H.; Yang, X.; Jiang, H.; Zhou, D.; Li, X.; Zhang, T.; Liu, J.; Wang, Q.; Qu, F. Hierarchical Core−Shell Heterostructure of Porous Carbon Nanofiber@$ZnCo_2O_4$ Nanoneedle Arrays: Advanced Binder-Free Electrodes for All-Solid-State Supercapacitors. *J. Mater. Chem. A* **2015**, *3*, 24082−24094.

(51) Huang, L.; Zhang, W.; Xiang, J.; Huang, Y. Porous $NiCo_2O_4$/C nanofibers replicated by cotton template as high-rate electrode materials for supercapacitors. *J. Materiomics* **2016**, *2*, 248−255.

(52) Jiang, H.; Ma, J.; Li, C. Hierarchical Porous $NiCo_2O_4$ Nanowires for High-rate Supercapacitors. *Chem. Commun.* **2012**, *48*, 4465−4467.

(53) Wang, H.; Gao, Q.; Jiang, L. Facile approach to prepare nickel cobaltite nanowire materials for supercapacitors. *Small* **2011**, *7*, 2454−2459.

(54) Li, L.; Peng, S.; Cheah, Y.; Teh, P.; Wang, J.; Wee, G.; Ko, Y.; Wong, C.; Srinivasan, M. Electrospun porous $NiCo_2O_4$ nanotubes as advanced electrodes for electrochemical capacitors. *Chem.—Eur. J.* **2013**, *19*, 5892−5898.